2012

Propagation of Kuroshio Extension Meanders between 143° and 149°E

Karen L. Tracey
University of Rhode Island, krltracey@uri.edu

D. Randolph Watts
University of Rhode Island, randywatts@uri.edu

Kathleen A. Donohue
University of Rhode Island, kdonohue@uri.edu

Hiroshi Ichikawa

Citation/Publisher Attribution

Tracey, K.L., D.R. Watts, K.A. Donohue, and H. Ichikawa, 2012: Propagation of Kuroshio Extension Meanders between 143° and 149°E. *J. Phys. Oceanogr.,* **42**, 581–601, https://doi.org/10.1175/JPO-D-11-0138.1
Available at: http://dx.doi.org/10.1175/JPO-D-11-0138.1

Propagation of Kuroshio Extension Meanders between 143° and 149°E

Propagation of Kuroshio Extension Meanders between 143° and 149°E

KAREN L. TRACEY, D. RANDOLPH WATTS, AND KATHLEEN A. DONOHUE

Graduate School of Oceanography, University of Rhode Island, Narragansett, Rhode Island

HIROSHI ICHIKAWA

Japan Agency for Marine-Earth Science and Technology, Yokosuka, Japan

(Manuscript received 9 August 2011, in final form 14 November 2011)

ABSTRACT

A two-dimensional array of current- and pressure-recording inverted echo sounders provided synoptic measurements of the upper and deep fluctuations in the Kuroshio Extension between 143° and 149°E with mesoscale resolution. Downstream-propagating meanders with periods of 3–60 days were always present between June 2004 and September 2005. Propagation speeds were estimated by two methods: spectral analysis of path displacements and complex empirical orthogonal functions (CEOF) analysis of along-path anomalies. The two methods produced similar results. Phase speeds increased smoothly from 10 km day^{-1} (0.12 m s^{-1}) for meanders with wavelengths and periods [λ, T] = [420 km, 40 days] to 35 km day^{-1} (0.41 m s^{-1}) for [λ, T] = [220 km, 6 days] meanders. This empirically derived dispersion relationship is indistinguishable from that obtained for Gulf Stream meanders downstream of Cape Hatteras. The deep ocean was populated with remotely generated, upstream-propagating eddies composed of a nearly depth-independent current structure. Upper meanders and deep eddies jointly spun up when they encountered each other with the deep eddy offset about a quarter wavelength ahead of the upper meander. Subsequently, as the upper and deep features moved past each other and the vertical offset changed, intensification ceased.

1. Introduction

The Kuroshio Extension is an eastward-flowing jet that forms after the Kuroshio leaves the coast of Japan. Its mean path is well known for the large-scale quasi-stationary meander pattern that forms with two crests near 144° and 150°E. Superimposed on the quasi-stationary pattern are shorter-wavelength meanders, which are alternatively called frontal waves, that propagate downstream along the front (Mizuno 1985; Hirai 1985; Kouketsu et al. 2005).

In the 1980s, two studies examined the characteristics of meanders using satellite infrared images of sea surface temperature (SST). Mizuno (1985) analyzed satellite infrared images collected during 1980 and 1982, focusing on the region of the Kuroshio Extension between 140° and 150°E. He illustrated three cases where the evolution of the surface temperature front was examined in 4–6 images, each spanning 2–4-week time periods. By tracking the downstream location of crests in successive images, he estimated the meanders had wavelengths of 200 km and phase speeds of 0.06–0.15 m s^{-1}. Hirai (1985) also used infrared images from a similar region, but he focused on frontal eddies. A frontal eddy differs from a meander in that it is a folded wave pattern characterized by a warm filament extending upstream from a meander crest and separated from the front by a pool of cold water (Lee et al. 1981; Bane et al. 1981). Frontal eddies evolve over time and translate downstream together with the meanders they trail behind. From the numerous frontal eddies that occurred between 1976 and 1983, Hirai (1985) determined propagation speeds of 0.35–0.45 m s^{-1}.

More recently, Kouketsu et al. (2005) reported on an ambitious four-ship survey of intermediate-depth meanders. In May–June 2001 they conducted high spatial resolution (~5 km) towed hydrographic observations and acoustic Doppler current profiler observations in the Kuroshio Extension. Subsurface at the 400–800-m depth of isopycnals associated with the intermediate layer, the meanders were larger amplitude than in the

Corresponding author address: Karen Tracey, Graduate School of Oceanography, University of Rhode Island, South Ferry Rd., Narragansett, RI 02882.
E-mail: ktracey@gso.uri.edu

DOI: 10.1175/JPO-D-11-0138.1

upper layer. Low salinity waters of Oyashio origin were systematically advected across the Kuroshio Extension front, southward from crest to trough and northward from trough to crest. Kouketsu et al. (2007) returned in September 2002 to determine the three-dimensional structure of the meanders, accounting for the effects of propagation upon the shipboard sampling that spanned more than half a wave period. They estimated a wavelength of ~200 km and a downstream propagation speed of ~0.2–0.3 m s^{-1}. They found a vertical phase tilt consistent with baroclinic instability, and they calculated vertical velocities ~40 m day^{-1}.

The phase speeds reported by Mizuno (1985) and Kouketsu et al. (2007) are much slower than those reported for Gulf Stream meanders of similar wavelength (Kontoyiannis and Watts 1994; Lee and Cornillon 1996). Gulf Stream meanders with wavelengths $\leq$200 km propagated at speeds $\geq$0.45 s^{-1}. Subtle differences between the Kuroshio Extension and the Gulf Stream could lead one to expect that their meander characteristics might differ. With mean downstream velocities of 1.6–2.0 m s^{-1} at 50 m and 0.6–0.8 m s^{-1} at 700 m (Johns et al. 1995; Meinen et al. 2009), the Gulf Stream is faster and deeper reaching than the Kuroshio Extension with corresponding values of 1.4 and 0.45 m s^{-1} (Howe et al. 2009). Although well-developed southern recirculation gyres exist in both current systems, only the Gulf Stream has a strong northern recirculation gyre. Westward flow extends all along the New England slope region (Hogg et al. 1986), whereas in the Kuroshio Extension westward flow was only recently discovered in localized cells of north of the quasi-permanent meander troughs (Qiu et al. 2008; Jayne et al. 2009). The motivation for this paper was to understand if the discrepancies in the reported phase speeds are due to differences in the current systems or other causes.

In 2004, a large multi-institutional investigation was undertaken. Known as the Kuroshio Extension System Study (KESS), the project sought to understand the processes governing the variability of the Kuroshio Extension and its recirculation gyres (Donohue et al. 2008). The 2-yr KESS observational program consisted of a moored array and profiling floats. The moored component included a two-dimensional array of current- and pressure-recording inverted echo sounders (CPIES) and a line of tall moorings that spanned the jet and southern recirculation gyre. Each mooring was equipped with an upward-looking acoustic Doppler current profiler, a moored profiler, and several current meters below the main thermocline. These measurements mapped the time-varying velocity and density structure throughout the water column with synoptic mesoscale resolution.

This paper utilizes the twice-daily maps of the upper and deep ocean to examine the characteristics of meanders propagating downstream along the Kuroshio Extension front, focusing on fluctuations with periods shorter than 60 days. Two different approaches are used. First, meandering is characterized by north–south displacements of the path as was done for the Gulf Stream (Halliwell and Mooers 1983; Watts and Johns 1982; Tracey and Watts 1986; Kontoyiannis and Watts 1994; Lee and Cornillon 1996). Subsequently, it is characterized by examining the variability of geopotential-height anomalies along the slowly varying mean path itself. Empirical dispersion relationships (phase speed versus wavenumber) are constructed for both analyses. Maps of the near-bottom reference field show that the deep-ocean variability is dominated by external eddies that propagate into the KESS region from the northeast or east, thus tending to oppose or cross meanders in the upper jet (Greene 2010). The three-dimensional resolution of the KESS array permits evolution of the upper and deep fluctuations to be examined jointly.

2. Data

The KESS moored array (Fig. 1) focused on the first quasi-stationary meander crest and trough (Mizuno and White 1983; Tatebe and Yasuda 2001) of the Kuroshio Extension. The array of 46 CPIES, centered near 35°N, 146°E, monitored the Kuroshio Extension path and its recirculation gyre to the south from May 2004 through June 2006 (Donohue et al. 2008). The instruments were concentrated in a 525 km by 525 km region, with a nominal spacing of 88 km.

Donohue et al. (2010) provides a comprehensive description of how the KESS CPIES measurements of acoustic travel time, bottom pressure, and near-bottom velocity were used to produce mesoscale-resolving fields of temperature, specific volume anomaly, and velocity. The bottom currents also included the velocities measured by the deepest current meters on the tall moorings. The data were mapped using optimal interpolation onto a grid with 10-km resolution. Correlation-length scales appropriate for mapping the suite of variables were determined from the measurements. Gaussian functions with correlation lengths of 130 and 75 km were used for iteratively mapping the low-pass- and high-pass-filtered travel times, respectively, and 100 km was used for multivariate mapping of the bottom pressures and velocities. Maps were generated at 12-h intervals for the 2-yr period. The entire KESS region was mapped for the first 16 months; subsequently, as instruments failed, subregions were mapped from October 2005 to May 2006. The mapping procedure did no temporal smoothing;

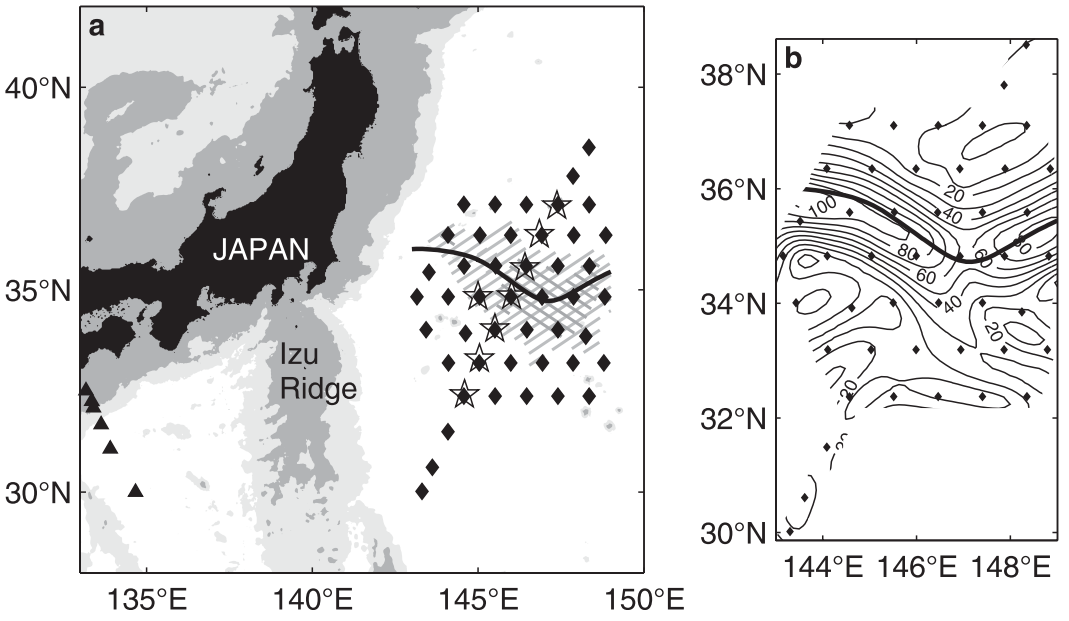

FIG. 1. The KESS study region was centered on the first quasi-stationary meander crest and trough of the Kuroshio Extension path east of Japan. (a) Locations of the CPIES and tall moorings are shown by black diamonds and stars, respectively. Mean path for June 2004–September 2005 is shown by bold line. Regions of 60-day high-pass-filtered η_{upper} with variance >0.1 m^2 are hatched and variance >0.2 m^2 are crosshatched. PIES along the ASUKA line are shown by black triangles. Bathymetry (2000- and 4000-m isobaths) is shaded gray. (b) Mean path superimposed on the surface velocity estimated by the CPIES array and averaged for the same 16-month period. Contour interval of the isotachs is 10 cm s^{-1}.

however, prior to mapping, the data were low-pass filtered with a cutoff period of 3 days. A detailed report of the processing and calibration of individual data records may be found in Kennelly et al. (2008).

This paper examines the variability of the Kuroshio Extension using maps of surface geopotential height relative to 5300 dbar ($\eta_{\text{upper}} = \Phi/g$) and the deep reference field at 5300 dbar ($\eta_{5300} = p/\rho g$) from 1 June 2004 through 30 September 2005, when the data coverage was most complete. Here, Φ is geopotential height of the surface relative to 5300 dbar, p is pressure anomaly nominally at 5300 dbar, ρ is density, and g is gravity. During the first 6 months, referred to here as the stable period, the Kuroshio Extension was in a weakly meandering state (Qiu and Chen 2005; Chen et al. 2007). Subsequently, in late 2004, it transitioned into a vigorously meandering state. The Kuroshio Extension remained in this unstable state for the remainder of the experiment. The 10-month period from December 2004 through September 2005 is referred to as the unstable period.

The position of the Kuroshio Extension path was defined by the 3.9-m contour in the η_{upper} fields (see Fig. 3), which coincided with the velocity maximum of the surface jet (Fig. 1b). A single path was determined for each map; isolated segments due to detached rings were excluded. The geographic positions were converted to displacements in kilometers from 35°N. In all, 974 paths were obtained with a temporal sampling interval of $\delta t = 0.5$ days. The mean path of the Kuroshio Extension during the first 16 months is shown in Fig. 1.

In the following sections, meandering of the Kuroshio Extension is characterized first by the variability of the north–south path displacements and subsequently by the variability along the slowly varying mean path itself. Characteristics of downstream-propagating meanders were calculated either from cross-spectral properties or from complex empirical orthogonal functions (CEOFs) [Hannachi et al. (2007) provides a comprehensive review of empirical orthogonal functions].

For the path-displacement analysis, it was necessary to remove multivalued segments that occurred along a meridian when the Kuroshio Extension became highly convoluted. Nearly one-quarter of the paths during the unstable period had multivalued segments. These segments were converted to a single value following the procedure described by Lee and Cornillon (1996). The multivalued segment was replaced by a single point that was midway between the easternmost and westernmost extent of the ''S shaped'' path and midway between its northernmost and southernmost extent. The resulting paths consist of single-valued segments. Although this procedure eliminates multivalued segments, it still

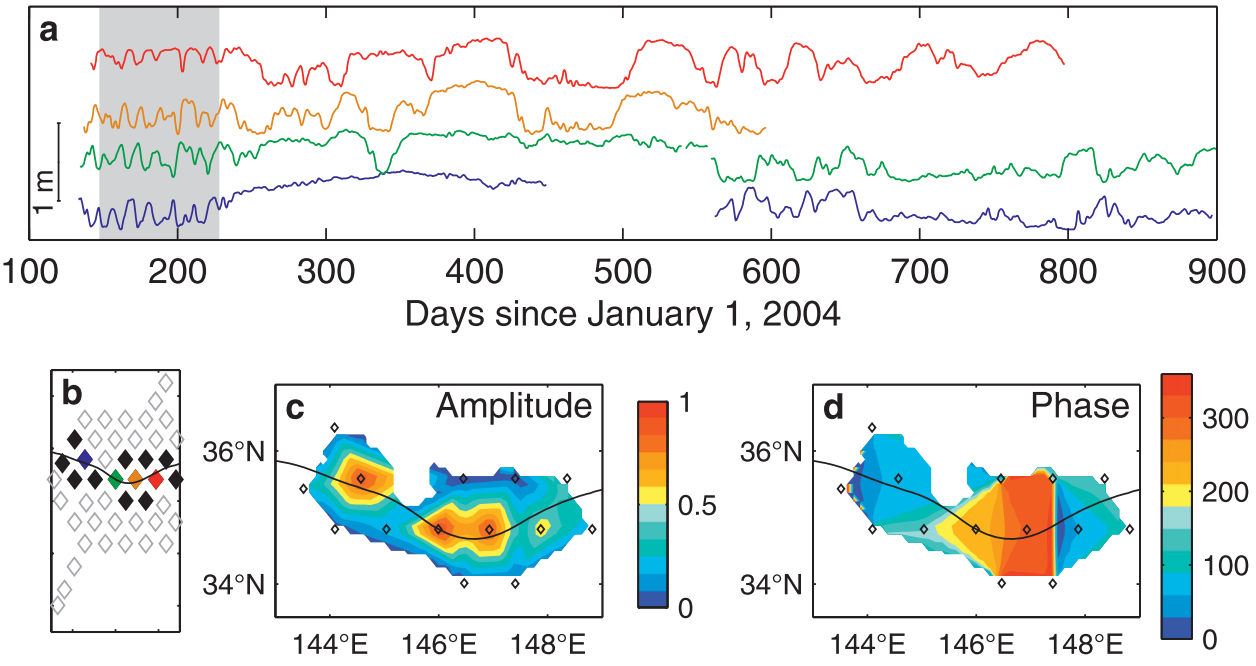

FIG. 2. (a) Geopotential-height records η_{upper} at four sites, color coded by location. Meanders with periods of about 12 days are evident during summer 2004 (gray shading). (b) CEOF analysis was run on the geopotential-height records at 14 sites shown by the solid diamonds near the mean path of the Kuroshio Extension (black line). Color-coded locations in (a) shown in (b). (c) First mode CEOF spatial amplitude (normalized) and (d) phase (degrees) exhibit high variance along the path and eastward propagation.

leaves abrupt large shifts of the path that arise from the passage of steep meanders or ring separations. These abrupt shifts can produce time series that are not stationary, and Fourier transforms will perform poorly on these records. Examining the variability as a function of along-path distance eliminated the difficulties associated with multivalued segments and large path shifts.

Coincident with KESS, several PIES and current meters were deployed along the Affiliated Surveys of the Kuroshio off Cape Ashizuri (ASUKA) line (Book et al. 2002; Kakinoki et al. 2008) and along 30°N by Japanese scientists. Figure 1 shows the six PIES sites along the ASUKA line that were occupied from July 2004 through late September 2006. The raw data files were obtained online (http://www.jamstec.go.jp/iorgc/ocorp/ktsfg/data/index.html) and processed with our software (Kennelly et al. 2007) to produce 3-day low-pass-filtered records of travel time and pressure. Fluctuations in travel time arise from the passage of Kuroshio meanders and their spectral properties will be examined later.

New Generation Sea Surface Temperature for Open Ocean (NGSST-O) provides quality-controlled, cloud-free, daily maps of SST by merging observations from several satellites (Sakaida et al. 2009). The high-spatial-resolution (0.05° grid) maps are available online (http://www.ocean.caos.tohoku.ac.jp/~merge/sstbinary/actvalbm.cgi).

3. Meander propagation: Path-displacement method

Strong fluctuations were observed in the geopotential-height records at several CPIES sites during the summer of 2004 (shaded gray in Fig. 2a). These fluctuations oscillated with periods of 10–15 days and the associated phase lags increased with distance downstream of Japan. CEOFs were computed using the 3-day low-pass-filtered geopotential-height records at the 14 CPIES sites closest to the mean path of the Kuroshio Extension during this time period. The first CEOF mode (Figs. 2c,d) accounted for over 60% of the total variance, with the second mode accounting for about 16%. Maximum spatial amplitude occurred along the mean axis of the jet. The sense of the phase lags indicates that the meanders propagate downstream.

The passage of one of these meanders through the KESS array is shown in a sequence of maps of the upper and deep fields (Fig. 3, top). The 3.9-m contour of η_{upper} lies within the central portion of the front, and this contour was used to define the path of Kuroshio Extension in this study.

Time series of the position where the 3.9-m contour intersected five longitudes are plotted in Fig. 4a. Displacements are shown for the first 6 months (stable period) when all the segments were single valued. The summer

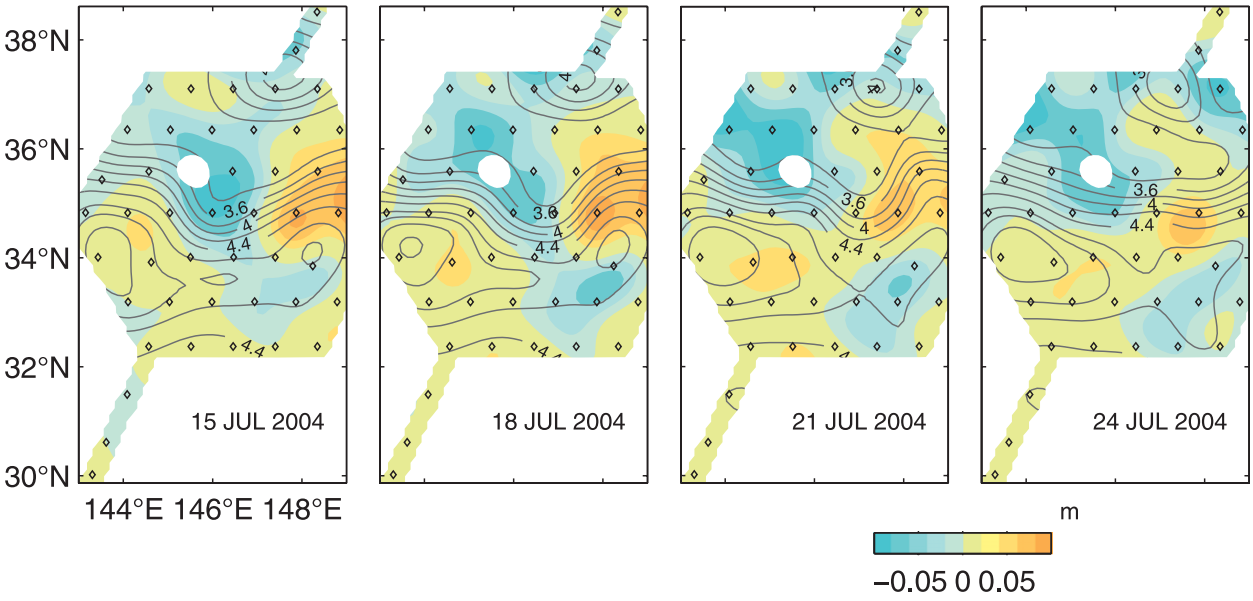

FIG. 3. A meander propagating eastward through the KESS array. Deep reference field η_{5300} is color shaded and η_{upper} is contoured with 0.2-m interval. Regions with higher mapping error are masked.

2004 meanders are readily apparent as peak-to-peak lateral displacements of about 50 km with periods near 10 days. Additionally, fluctuations at a variety of periods are observed through the end of November that can be tracked downstream.

Spectra of these displacements were computed using the Welch method. To focus on fluctuations with periods shorter than 60 days, the records were broken into segments consisting of 182 twice-daily values, overlapped by 50%, and scaled with a Hanning window. Additionally, three adjacent frequency bands were averaged to increase statistical confidence.

The spectra are plotted in variance-conserving form in Fig. 4b. Downstream growth in variance is evident: at periods longer than 10 days, the variance more than doubles in the first 90 km downstream between 144° and 146°E. The variance remains fairly constant at the central longitudes and then decreases at the eastern edge, particularly at periods between 10 and 20 days. Visual peaks occur near periods of 7 and 4.5 days at all longitudes, 13–18 days at the western longitudes, and 30–45 days at the eastern longitudes.

Coherence and phase delays, calculated between three pairs of longitudes (Figs. 4c,d), were used to determine meander phase speeds. The upstream and downstream pairs are separated by 1° longitude, and the third pair spans 3° longitude. The sense of the phase lag $\delta\phi$ is such that the propagation is eastward. The calculations were performed only using the values where the coherence exceeded the 95% significance level. Phase speeds were determined as $c = \delta x \cdot (2\pi f/\delta\phi)$, where f is frequency and δx is the distance in kilometers the meanders traveled along the 6-month-mean position of the Kuroshio Extension between longitude pairs. The phase speeds are listed in Table 1 together with the estimated wavenumbers ($k = \delta\phi/\delta x$) and the corresponding wavelengths ($\lambda = 2\pi/k$).

The above procedure was repeated for the path displacements during the unstable period. Abrupt shifts of the path caused by the passage of large-amplitude meanders and ring-shedding events occurred often and yielded displacement records that were less than ideal for Fourier analyses. Indeed, the coherences calculated between longitude pairs did not exceed the 95% significance level, and so meander phase speeds during this period were not determined.

To examine fluctuations with periods longer than 60 days, the procedures were repeated using the full 16-month-long dataset. Calculations were performed using only pairs of longitudes west of 147°E to minimize the effects of abrupt path shifts. The records were broken into overlapping segments of 487 values, which resulted in fewer degrees of freedom and coherences that were not significant at the 95% level. Nevertheless, wavelengths and phase speeds were estimated for meanders with periods of 121 days; these are listed in Table 1 for the 145°–146°E longitude pair.

4. Meander propagation: Along-path method

a. Tracking anomalies along the slowly varying mean path

With the KESS dataset, it is possible to avoid the above abrupt path shifts by examining the variability of

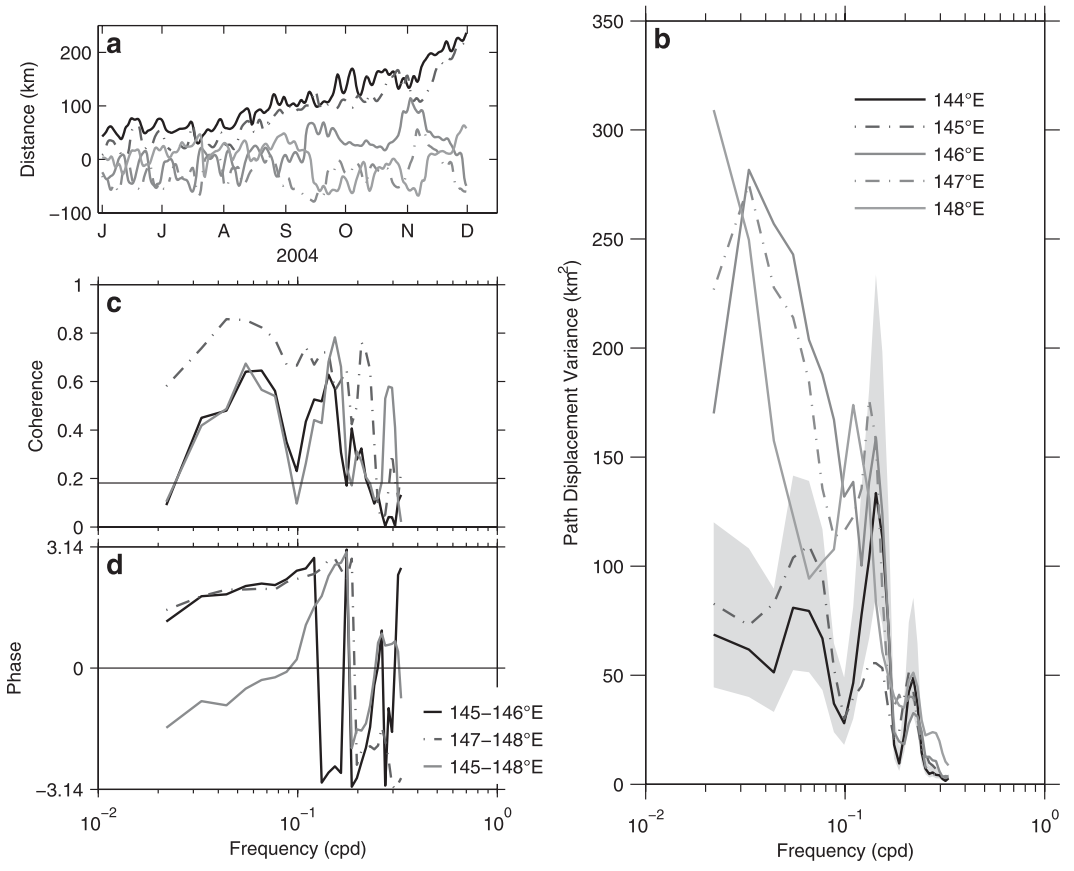

FIG. 4. Meander characteristics during the stable period. (a) Displacements of the Kuroshio Extension path determined from the twice-daily mapped fields at five longitudinal sections. (b) Ensemble- and band-averaged power spectra of the path displacements shown in (a). The 95% confidence interval for the 144°E spectrum (solid black) is shaded gray. (c) Coherence and (d) phase between downstream section pairs. The horizontal line in (c) indicates the 95% significance level.

geopotential height along the mean path for time intervals as described below. High and low η_{upper} correspond to the crests and troughs of path displacements, respectively. Meander propagation can be examined by analyzing the propagating η_{upper} features.

First, it was necessary to choose an appropriate Kuroshio Extension path. Occasionally, the path shifted greatly because of large-amplitude meanders or ring-shedding events. Subsequently, its position would remain relatively steady until the next strong event shifted it again. These intermittently quasi-steady paths differed sufficiently from one to another that it was not appropriate to choose a single mean pathway along which to track η_{upper} perturbations. Seven time intervals, with durations of 40 to over 90 days, were selected when the path was quasi steady. Mean paths were calculated separately for each interval. These paths ranged in length from 570 km when the Kuroshio Extension was relatively straight to over 1000 km when it had a steep crest–trough pattern.

Geopotential-height anomalies were extracted from the upper-ocean maps along the appropriate mean path for each 0.5-day time step. Examples of along-path η_{upper} are shown in Fig. 5 for 30 days in the spring of 2005 together with the corresponding path displacements for the same dates.

Likewise, η_{5300} anomalies were extracted from the deep-ocean fields along the identical mean paths for the same time blocks. These will be examined for deep signatures associated with the upper meanders.

For this analysis, η_{upper} and η_{5300} were bandpass filtered in four period bands: 60–30 days, 30–15 days, 15–7.5 days, and 7.5–3.75 days. Examples of the bandpass-filtered along-path η_{upper} are also shown in Fig. 5. Because the 7.5–3.75-day signals are weak compared with the other bands, they are not illustrated here. Individual meanders can easily be tracked from the western to eastern edges of the domain, even as they propagate through the steep meander trough.

Hovmöller diagrams (Fig. 6) display concisely the bandpassed along-path η_{upper} and η_{5300} anomalies for

TABLE 1. Propagation speeds from path-displacement analyses for line pairs 145°–146°E, 147°–148°E, and 145°–148°E. Coherences exceeded the 95% significance level in all cases but $T = 121.7$ days.

		λ (km)			k (10^{-2} rad km^{-1})			c (km day^{-1})		
T days	f cpd	145°E 146°E	147°E 148°E	145°E 148°E	145°E 146°E	147°E 148°E	145°E 148°E	145°E 146°E	147°E 148°E	145°E 148°E
121.7	0.008	672			0.01			5.5		
45.5	0.022		406			1.55			8.9	
30.3	0.032	375	328	359	1.67	1.92	1.75	12.4	10.8	11.8
22.8	0.044	366	300	366	1.72	2.09	1.72	16.1	13.2	16.1
18.2	0.055	329	299	339	1.91	2.10	1.86	18.1	16.5	18.6
15.2	0.066	319	297	326	1.97	2.12	1.93	21.1	19.6	21.5
13.0	0.077	325	300	322	1.93	2.10	1.95	25.0	23.1	24.8
11.4	0.088	304	274	315	2.07	2.30	2.00	26.7	24.1	27.7
10.1	0.099	277	264		2.27	2.38		27.4	26.2	
9.1	0.110	271	257	263	2.32	2.44	2.39	29.8	28.3	28.9
8.3	0.121	245	250	247	2.57	2.51	2.54	29.6	30.3	29.9
7.6	0.132	211	237	239	2.98	2.65	2.63	27.8	31.2	31.5
7.0	0.143	196	218	225	3.21	2.88	2.80	27.9	31.1	32.1
6.5	0.154	187	216	217	3.36	2.91	2.89	28.8	33.2	33.4
6.1	0.165	196	239	216	3.21	2.63	2.91	32.3	39.4	35.6
5.7	0.176		265	210		2.37	3.0		46.7	36.8
5.4	0.187	218	215		2.88	2.92		40.7	40.2	
5.1	0.198	204	162	177	3.09	3.89	3.55	40.3	32.0	35.1

the seven time blocks. They clearly demonstrate the prevalence of meanders propagating through the KESS region during both the stable and unstable periods. With few exceptions, the η_{upper} anomalies (contour lines) slope from the upper left to the lower right, the signature of downstream propagation. The meander sequence that was shown in Fig. 3 appears as one of several such events in the 15–7.5-day period band (bottom) in the first time block (June–September 2004). Downstream-propagating meanders are present in each time block, exhibiting variable amplitudes in each period band.

One notable exception occurs in time block 3 (December 2004), when the contours slope from the lower left to the upper right at along-path distances of 600–1000 km, ostensibly indicating upstream propagation. This is an artifact; because the mean path forms a steep trough with a narrow neck (map inset), meanders entering the trough simultaneously intersect the path exiting the trough.

b. Deep eddies translating downstream and upstream

Many of the downstream-propagating η_{upper} anomalies are accompanied by downstream-propagating η_{5300} anomalies (colored shading in Fig. 6), indicating that meanders have a deep signature. The η_{5300} highs (red shading) slope from the upper left to the lower right, parallel with η_{upper} highs (gray contours). Similarly, the deep lows (blue shading) translate downstream with lows in the upper ocean (black contours). Clear examples of joint propagation in Fig. 6 are the 15–7.5-day meanders in time block 1 and the 30–15-day meanders in time block 2.

In other cases, strong deep eddies appear to propagate upstream (sloping from the lower left to the upper right) and pass beneath the meanders of the upper jet. The map sequences (not shown) upon which these Hovmöller plots are based show that deep eddies approach from the northeast and translate southwestward across the upper-jet path. Greene (2010) examined these eddies in the most energetic 60–30-day period band and identified them as nearly depth-independent, topographically controlled features that were generated farther to the east at the Shatsky Rise. In the Hovmöller plots, these eddies project onto the Kuroshio Extension path as η_{5300} anomalies with upstream propagation. Cases of upstream propagation are evident in all three period bands, although they are more common at longer periods. In Fig. 6 clear examples occur during time block 1 for both the 60–30-day (top) and 30–15-day (middle) bands.

c. Meander propagation speeds by CEOF

The method to determine propagation speeds of meanders in four period bands using bandpass-filtered along-path η_{upper} data is described next. Complex empirical orthogonal functions were computed for η_{upper} in each of the seven time blocks and each period band separately. The output of the CEOF consists of spatial amplitude and phase, and temporal amplitude and phase for each mode. The first CEOF mode in each time block accounted for 70%–98% of the total variance for the three longer-period bands. For the 7.5–3.5-day band, this mode explained 46%–71% of the variance.

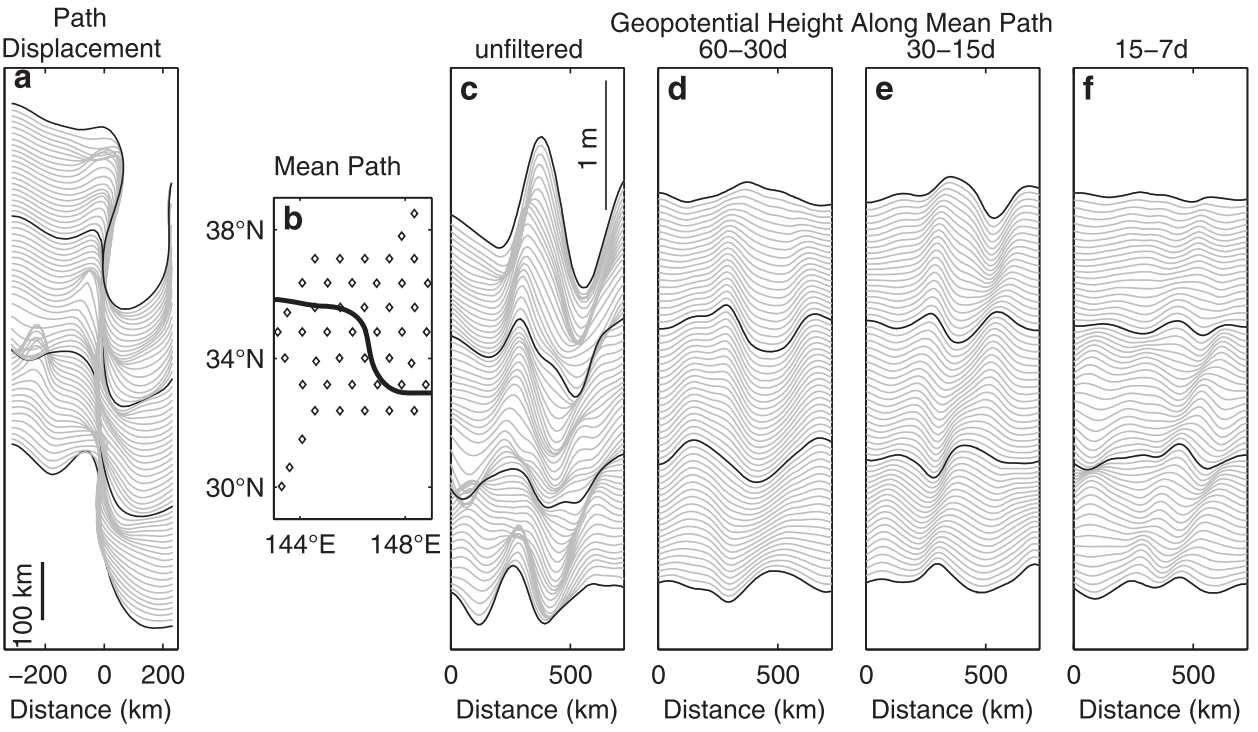

FIG. 5. Path displacements and along-path η_{upper} from mid-April to mid-May 2005 when a meander trough steepened. (a) North–south displacements in kilometers measured from 35°N. η_{upper} as function of distance along (b) the mean path of the Kuroshio Extension: (c) unfiltered and (d)–(f) bandpass filtered in three period bands, (d) 60–30 days, (e) 30–15 days, and (f) 15–7.5 days. Line origins are shifted such that time increases upward in each panel. Every 10th day is plotted in black. The η_{upper} scale in (c) also applies to (d)–(f).

First, an average period was needed to represent each frequency band. The slope of the temporal phase provides an estimate of the mean meander frequency ω during the time block. Slopes were calculated for each time block separately using the unwrapped temporal phase of the first CEOF mode. The inverse slopes yielded seven estimates of meander period ($T = 2\pi/\omega$), which varied by ±10% from block to block. The average periods and their standard deviations are listed in Table 2.

Next, an average wavelength was determined for each frequency band using the first CEOF mode spatial phase. Wavenumber k was calculated as the slope of the unwrapped phase, and wavelength $\lambda = 2\pi/k$ was calculated from its inverse. The slope and the 95% confidence intervals were determined by linear regression of the spatial phases of the seven time blocks. For this calculation, only along-path segments with phases indicating downstream propagation were included. The wavenumbers are listed in Table 2 together with the corresponding wavelengths and their uncertainties.

Phase speeds $c = \lambda/T$ for downstream-propagating meanders from along-path η_{upper} are listed in Table 2. The speeds more than tripled from 9.6 km day^{-1} for meanders with wavelengths and periods of [λ, T] = [418 km, 43 days] to 36.2 km day^{-1} for meanders with [λ, T] = [227 km, 6.3 days]. Maximum and minimum propagation speeds listed for each frequency were calculated using the ranges listed for the corresponding period and wavelength.

d. Robustness of the method

The choice of start and end dates of the time blocks can affect the phase-speed estimates. When the averaging dates change, the mean paths change. As a prerequisite for estimating meander phase speeds accurately, the instantaneous paths should not deviate more than a current width (80 km) from the mean path for that block to ensure that η_{upper} anomalies along the front are tracked. As a test of the robustness of the technique, mean paths were recalculated for only two time blocks, the 6-month stable period and the 10-month unstable period. The CEOF analysis was repeated using the η_{upper} anomalies along those paths and phase speeds were recalculated. Bandpass filtering insured that the analyzed periods would be consistent.

For the stable period, the mean path closely resembled those of the time blocks 1 and 2 in Fig. 6, and the resulting Hovmöller diagrams for all period bands were also similar. The first CEOF mode accounted for 60%–80% of the total variance in the four period bands.

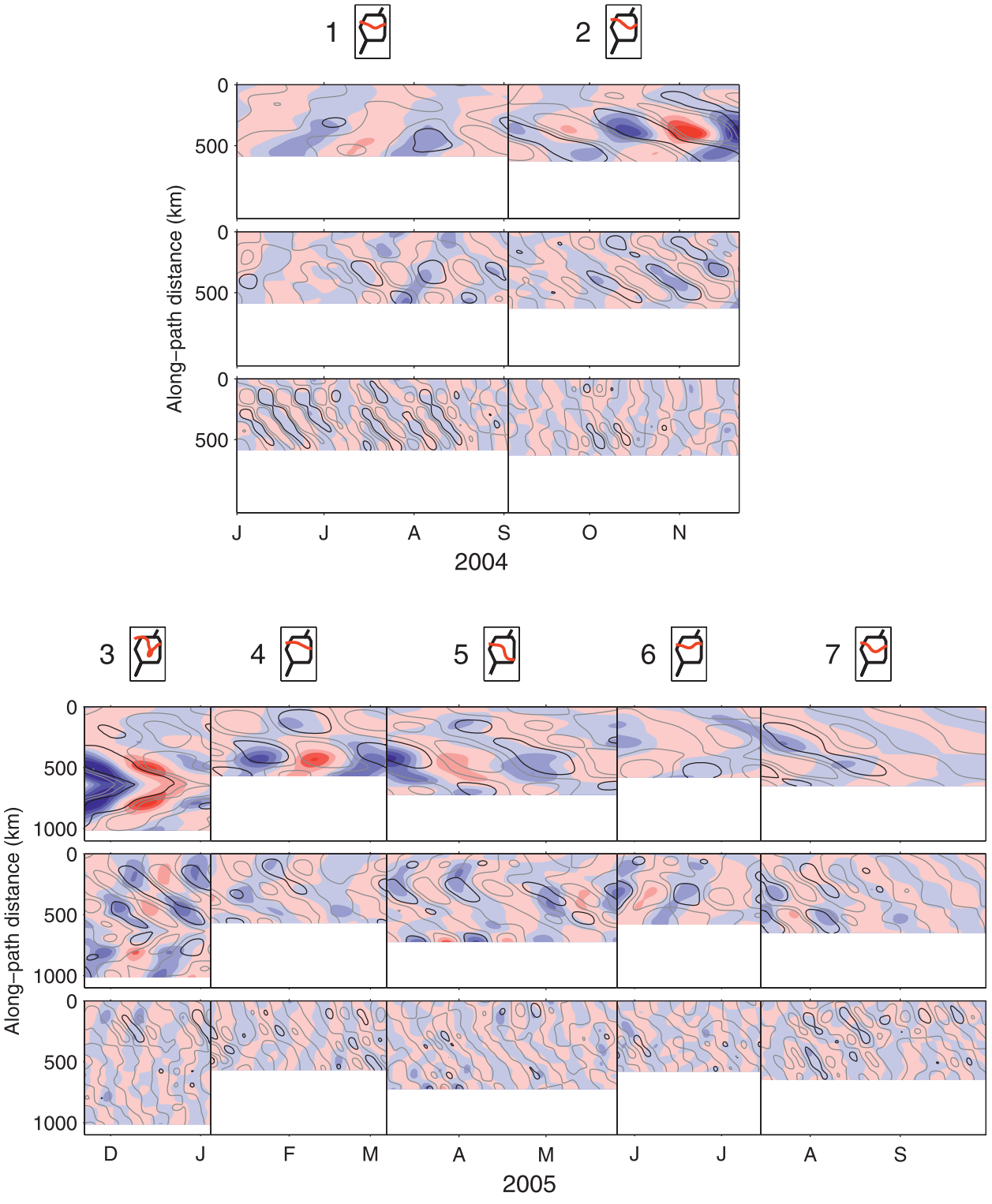

FIG. 6. Hovmöller diagrams of bandpass-filtered η_{upper} and η_{5300} as functions of along-path distance and time. The mean path during each time block is shown (red line). The three period bands shown are (top) 60–30 days, (middle) 30–15 days, and (bottom) 15–7.5 days. The time blocks are grouped into (upper) stable (blocks 1 and 2) and (lower) unstable periods (blocks 3–7). η_{upper} is contoured with positive anomalies gray and negative black; for visual clarity, only −0.1-, 0-, and 0.1-m contours are plotted. η_{5300} is color shaded with positive anomalies red and negative anomalies blue using a 0.02-m contour interval.

TABLE 2. Average propagation speeds for along-path η_{upper} determined from CEOF analyses. Also listed are the standard deviations for period T, 95% confidence intervals for wavenumber k, the corresponding uncertainties for wavelength λ, and the minimum and maximum values for phase speed.

T (days)	k (rad km^{-1})	λ (km)	c (km day^{-1})
43.5 ± 3.7	0.0150 ± 0.0020	418 ± 60	9.6 (7.8–12.1)
22.0 ± 3.1	0.0170 ± 0.0004	370 ± 8	16.8 (15.1–19.1)
10.9 ± 1.2	0.0212 ± 0.0005	297 ± 7	27.1 (25.3–30.1)
6.3 ± 0.5	0.0277 ± 0.0009	227 ± 7	36.2 (34.1–37.5)

For the two longest-period bands, the wavenumbers and phase speeds fell within the estimated errors shown in Table 2. For the shorter-period bands, the values slightly exceeded the predicted ranges, and the wavelengths and phase speeds were 5%–10% higher than those tabulated.

The mean path for the unstable period differed substantially from those in Fig. 6 for time blocks 3–7. The Hovmöller diagrams showed that similar η_{upper} anomalies were tracked, but for shorter distances. The first CEOF mode explained 50% of the variance in the two longest-period bands and only 30%–45% in the shorter bands. The estimated phase speeds agreed within 12% of those listed in Table 2.

5. Meander growth

In Fig. 6, the meanders do not grow systematically downstream. Instead, in isolated intervals (~1 month) some packets of meanders grow downstream for 100–200 km and then decay farther downstream in 100–200 km. Case studies presented next show the circumstances under which growth takes place.

Two cases when the meanders exhibited nearly continuous growth as they transited the KESS region are illustrated in Fig. 7. The Hovmöller diagrams from Fig. 6 for the 30–15-day meanders in time block 2 and the 60–30-day meanders in time block 5 are repeated with different contouring intervals. Superimposed are solid lines (labeled a–d) that track individual meander crests and troughs as they progress downstream depicting a constant phase speed. As the meanders pass through the array, amplification is exhibited by the increase in contours.

The η_{5300} anomalies (color shaded) translate downstream at the same rate of speed as the upper meanders. They, too, amplify downstream in these cases. Careful examination reveals that the upper and deep features parallel each other, but a phase offset exists between them with the deep anomalies preceding the upper meanders.

An alternate view is provided by Fig. 7 (bottom) in which η_{upper} and η_{5300} at three fixed locations along the mean path are plotted as a function of time. A train of meander crests and troughs passes each location. Black lines connect the same meander crests (Fig. 7a,c) and troughs (Fig. 7b,d) highlighted in the Hovmöllers when they arrive at those locations. The upper and deep features fluctuate together, but the deep anomalies arrive at each location ahead of those in the upper ocean. For the 60–30-day meanders, the phase offset is about ¼ of a wave period. For the 30–15-day meanders, it is smaller and more variable. The sense of these phase offsets (tilting westward with height above the seafloor) is favorable for the release of potential energy, allowing the upper and deep features to jointly spin up. The amplitudes of crest a and trough b more than double in a span of 300 km over the course of 20 days. Similarly, crest c and trough d are 1.5 times stronger after a 25-day interval.

Caution must be exercised when using these diagrams to quantify meander growth. Plan-view maps (Fig. 7) of the bandpass-filtered η_{upper} and η_{5300} show that the anomaly extrema did not always center upon the mean path. This was the case for crest c and trough d, so their magnitudes are underestimated. Offsets such as this were more common during time blocks 3 and 5, when steep troughs were developing and differences between the instantaneous and mean paths were more pronounced. For crest c and trough d, peak values were determined using the mapped fields and their ratios were recalculated. Fortuitously, the amplitude ratios remained unchanged in these two cases.

There are several other examples in Fig. 6 where the upper and deep anomalies propagate downstream together but do not grow. Most obvious are the 15–7.5-day meanders in time block 1. Instead of growing downstream, meander amplitudes decay. Time series of η_{upper} and η_{5300} at several locations (not shown) reveal that the upper and deep features remained aligned vertically as they transited the KESS array. The observed phase offsets of less than 1/30 of a wave period were not sufficient for joint intensification.

In Fig. 6, it is more common to find examples of the upper and deep fields crossing each other rather than translating together. For many of these cases, both the η_{upper} and η_{5300} anomalies modulate in intensity over short time and space scales. The case study highlighted in Fig. 8 typifies many such interactions between downstream-propagating upper meanders and preexisting deep eddies with an upstream component of translation. This case examines the 30–15-day meanders in time block 1. In the Hovmöller diagram in Fig. 8, the black lines trace the average translation downstream of the positions of the upper trough e and upper crest f. Instead of paralleling the upper meanders, the deep highs and lows cross them. Both the η_{upper} and η_{5300} anomalies vary in amplitude along the path. Features strengthen

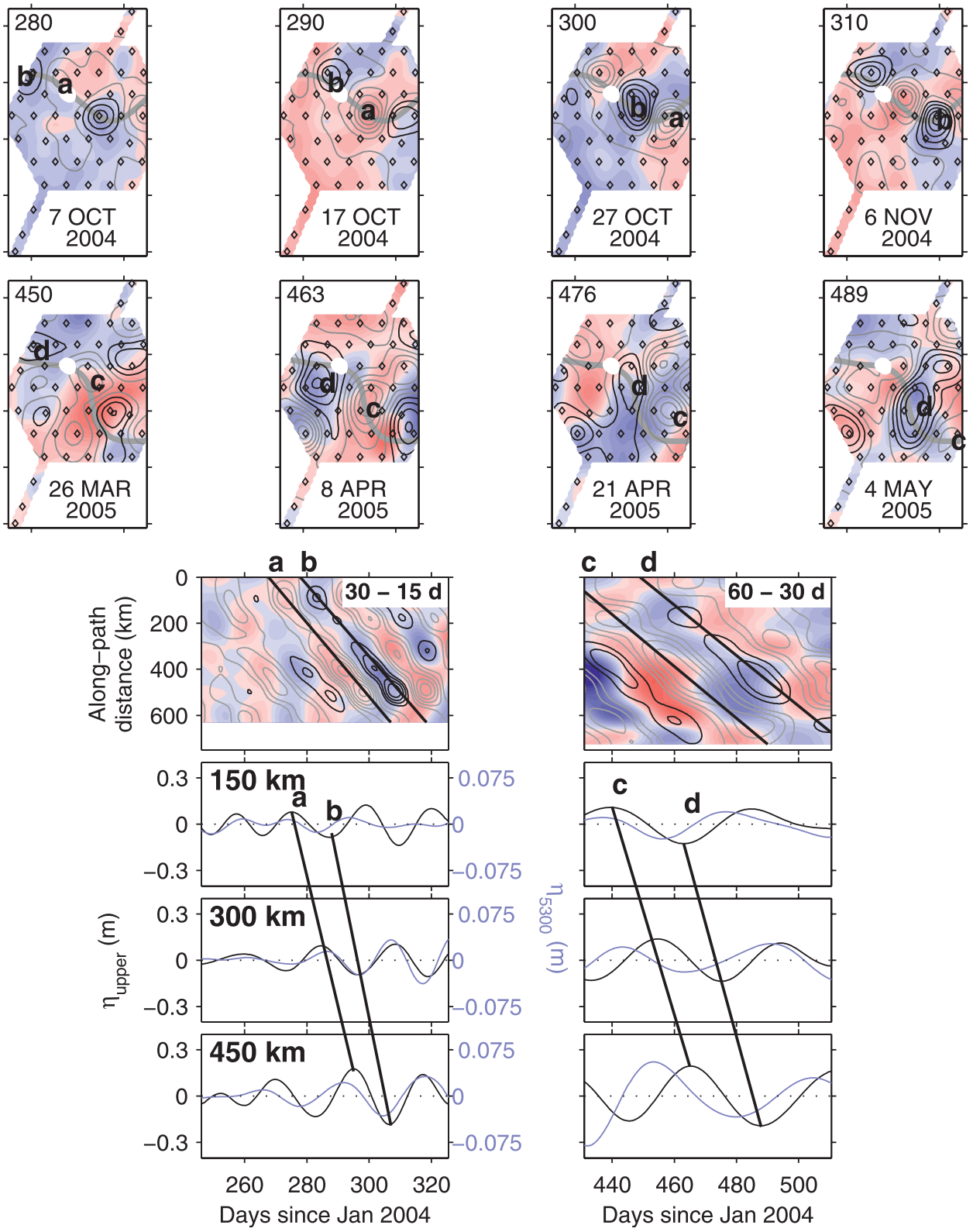

FIG. 7. Individual meander crests and troughs (a)–(d) amplify as they propagate downstream together when the vertical phasing is favorable. Bandpass-filtered upper and deep fields are shown in plan-view maps and Hovmöller diagrams with the same convention: η_{upper} (gray) and η_{5300} (red) meander crests (a, c, and f) and η_{upper} (black) and η_{5300} (blue) meander troughs (b, d, and e). Contour intervals are 0.05 m for η_{upper} and 0.005 m for η_{5300}. The yearday in the top-left corner of each map corresponds to the date shown. (bottom) Time series of η_{upper} (black) and η_{5300} (blue) at three locations along the mean path. The upper-ocean meanders are tracked downstream by black lines.

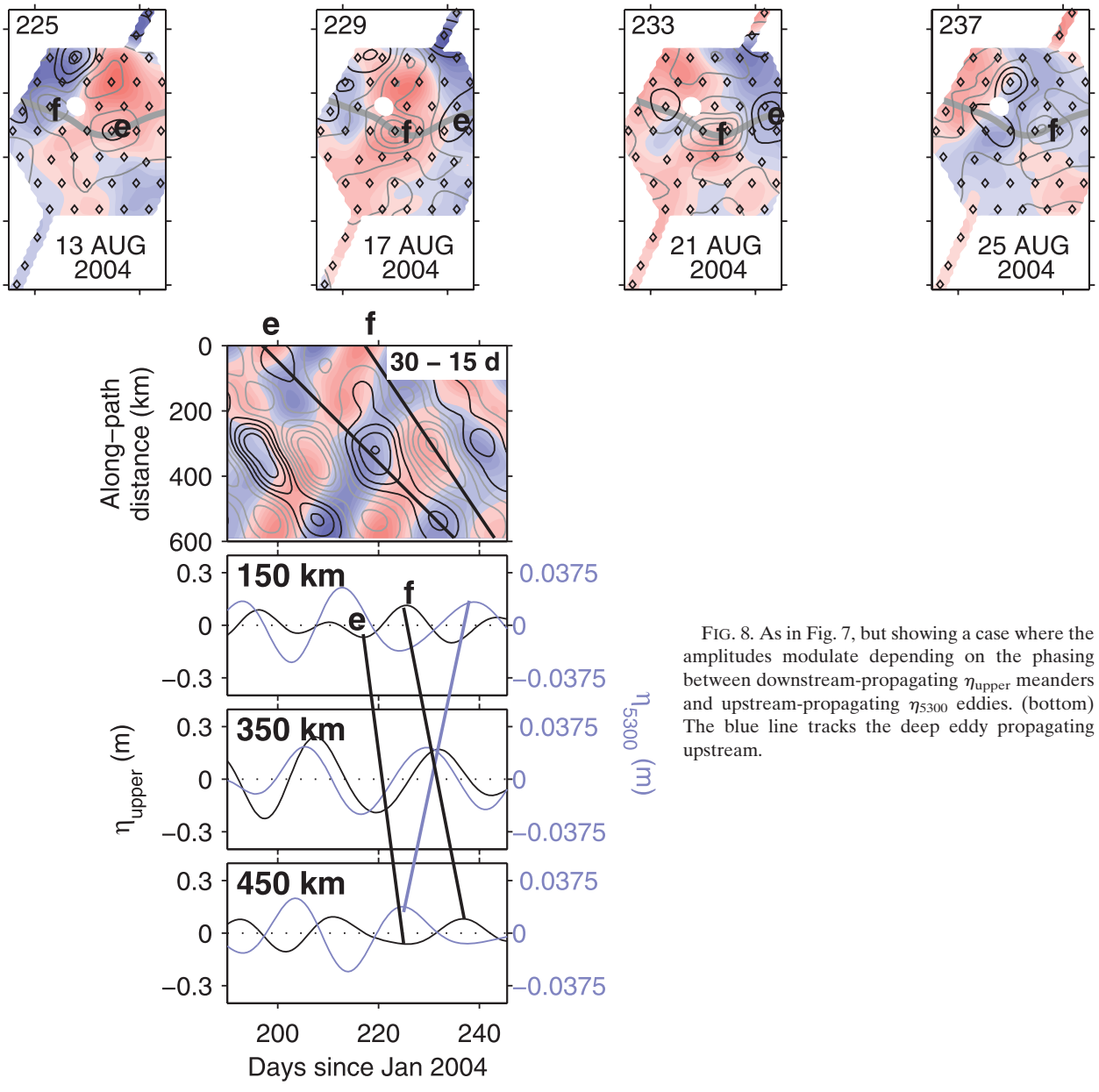

FIG. 8. As in Fig. 7, but showing a case where the amplitudes modulate depending on the phasing between downstream-propagating η_{upper} meanders and upstream-propagating η_{5300} eddies. (bottom) The blue line tracks the deep eddy propagating upstream.

where deep lows encounter upper troughs and where deep highs encounter upper crests. Conversely, the amplitudes decrease where the deep lows meet crests and deep highs meet troughs.

The maps and time series in Fig. 8 clarify why these intervals of amplification are short lived. On 13 August 2004 (day 225), trough e is located at a distance of 450 km along the mean path. It lies directly over a high anomaly in the deep ocean. Similarly, crest f, at the illustrated along-path distance of 150 km, overlies a deep low. The time series plotted for those locations show η_{upper} and η_{5300} are 180° out of phase on that date, and the Hovmöller shows both had weakened.

During the next 4 days, the upper trough and crest propagated downstream farther to the east. Meanwhile, the deep anomalies moved westward and a second deep low entered the study region on the eastern side. By 17 August (day 229), the deep high that had been beneath trough e was under crest f. The η_{upper} and η_{5300} records at a distance of 350 km, the approximate location of crest f, show the upper and deep positive anomalies are nearly aligned. They are phase shifted by about 1/6 of a wave period with the deep anomaly leading the upper. This alignment is favorable for growth, and the Hovmöller shows that crest f and the deep high jointly intensify. Because the upper and deep features are

moving in opposite directions, this favorable orientation is maintained for a brief period only and the intensification is short lived (4–8 days). By day 237, crest f, located 450 km downstream, encounters another deep low. The upper and deep anomalies are once again 180° out of phase and the features weaken.

6. Discussion

a. Resolving T, λ, c, and amplitude

Simulations were conducted to determine how well the KESS array detects propagating meanders. Meanders were generated analytically as propagating sine waves for a variety of periods, wavelengths, and phase speeds on a finescale grid for 100 days. Meander amplitudes were modulated with time. The daily analytic fields were subsampled at the CPIES locations and mapped with the same procedures used for the KESS data. Meander periods, wavelengths, and phase speeds were determined from both the analytic and mapped fields using the along-path method described in section 4. A detailed description of the simulations is given in the appendix. For our array spacing and mapping correlation-length scale, the simulations show that meander periods and frequencies are resolved accurately, with the mapped and analytic periods differing by less than 0.04%. For meanders with wavelengths $\lambda \geq 180$ km, mapped wavenumbers are well resolved when averaged along the path for distances of 300–400 km; wavelengths were either underestimated or overestimated by less than 1.5%. Meanders with $\lambda < 180$ km are poorly resolved by the KESS array. The deduced phase speeds are as well resolved as T and λ. Amplitudes are adequately resolved (mapped ≥70% of analytic) when $\lambda \geq 250$ km. For shorter-wavelength meanders ($180 \leq \lambda \leq 220$ km), however, the shapes of the mapped anomalies became distorted and the amplitudes ranged between 30% and 300% of truth.

b. Possible upstream origin

Travel-time measurements from the ASUKA line were used to investigate the origins of the meanders observed in the KESS region. Satellite altimetry shows that during much of 2004 and 2005 the Kuroshio was located over the three sites closest to the coast (Fig. 1). Therefore, variations in the travel times measured at those sites can be interpreted as fluctuations in the Kuroshio path caused by meanders. Spectra were computed for those three records in the same manner as spectra for the KESS path-displacement records to examine the 3–60-day fluctuations. The travel-time spectra from the two sites farther offshore (PA021 and PA031 in Fig. 9) exhibit visual peaks at 4.5 days, 7–10 days, and 45 days, and the spectrum from the most inshore site (PA011) has a peak at 11–15 days. These peaks occur at similar periods to those obtained for the path displacements in the KESS region (Fig. 4). Similarities in spectral properties between the two study regions suggest an upstream origin for the meanders observed during KESS. This is consistent with previous research (Ambe et al. 2004) that tracked eastward-propagating meanders over the Izu Ridge as far east as 143°E by combining data from satellite altimeters and surface drifters.

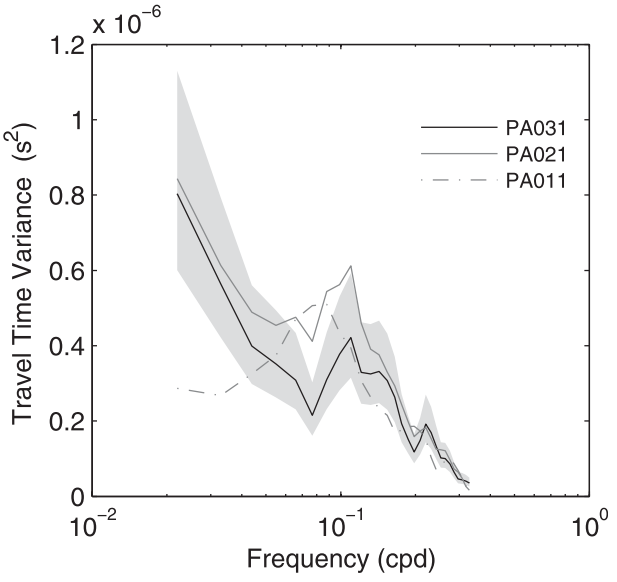

FIG. 9. Variance-preserving spectra of travel time measured at three sites along the ASUKA line. The 95% confidence interval for the PA031 spectrum (solid black) is shaded gray.

c. Deep eddy propagation

To investigate the deep eddies further, CEOFs were computed using the mapped fields of bandpass-filtered η_{5300} to examine the spatial structure of phase propagation. The first CEOF mode accounted for 54% of the variance in the 60–30-day period band and 45% and 44% in the 30–15-day and 15–7.5-day period bands, respectively. In all three period bands, the second CEOF mode accounted for 23%–26% of the variance. The first CEOF mode amplitudes and phases are shown Fig. 10 for the three period bands.

The 60–30-day band (Fig. 10, top), originally shown in Greene (2010), exhibits a phase propagation from the north-northeast to the south-southwest with a maximum spatial amplitude near the first quasi-stationary meander trough of the Kuroshio Extension. He identified these as topographically controlled features with phase speeds of 12–14 km day^{-1}. He also examined the bottom

pressures from the Ocean General Circulation Model for the Earth Simulator [OFES; operated by Japan Marine Science and Technology Center (JAMSTEC)] to determine the source of the deep eddies. He found a ridge of high variance extending from the KESS array eastward to the Shatsky Rise near 158°E. The model pressures also exhibited a westward phase propagation. Greene (2010) determined that the deep eddies originated when the meandering Kuroshio Extension encountered the Shatsky Rise, because the topographic slopes there are favorable for vertical coupling.

Both the 30–15-day and 15–7.5-day bands also exhibit phase propagation with a westward component. In the 30–15-day band (Fig. 10, second row), spatial amplitude is highest within and north of the Kuroshio Extension, and phase propagation is from the northeast to the southwest. Phase speeds were estimated to be about 23 km day^{-1}. In the 15–7.5-day band (Fig. 10, third row), spatial amplitudes are fairly uniform throughout the array and phase propagation is primarily westward; phase speeds of ~46 km day^{-1} were estimated. The deep pressures from two models, OFES and the Hybrid Coordinate Ocean Model (HYCOM; developed by a multi-institutional consortium) in these two period bands are currently being investigated (S. Zamorski and K. Donohue 2011, personal communication). CEOFs of the model pressures show westward propagation in all three period bands. Both models show a region of high variance in the 30–15-day band stretching from the KESS array to the Shatsky Rise. This suggests that the deep eddies in this period band may have a similar origin as those in the 60–30-day band. It is interesting to note that the phase of the 15–7.5-day band (Fig. 10, third row) has a northward component along the eastern edge of the array. A cluster of seamounts is located in this southeastern corner, and perhaps interactions between with the meandering Kuroshio Extension or with cold-core rings that occur there generate deep eddies.

d. Upper-ocean meander dispersion curve

Empirical relationships between phase speed and wavenumber determined from the two methods (spectral analysis of path displacements in Table 1 and CEOF analysis of along-path anomalies in Table 2) are compared in Fig. 11. The two dispersion-relation estimates are consistent with each other, although the along-path-method phase speeds tend to be slightly faster. Phase speeds increase smoothly from roughly 5 km day^{-1} for meanders with nominal wavelengths and periods of [670 km, 120 days] to 10 km day^{-1} for wavelengths and periods of [420 km, 40 days], and reach 35 km day^{-1} for meanders with wavelengths and periods of [220 km, 6 days]. The agreement between these relationships

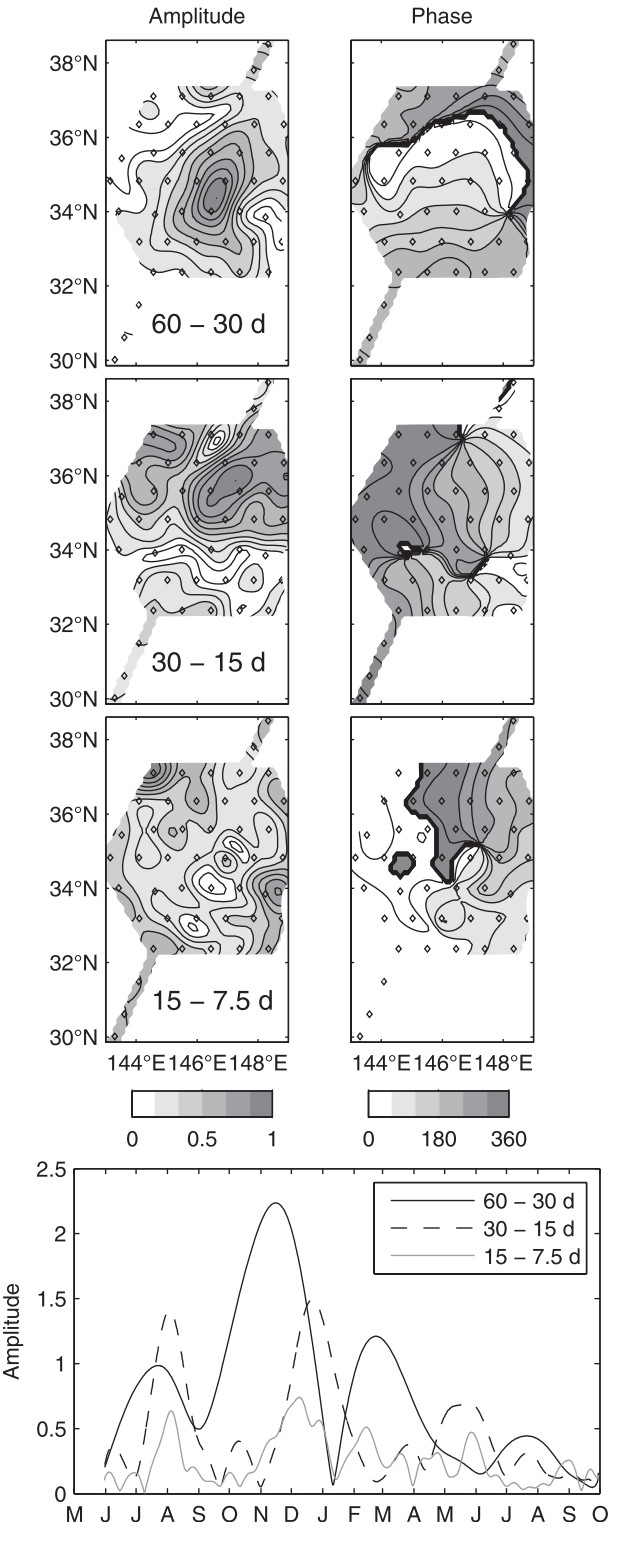

FIG. 10. First mode CEOFs for 60–30-day, 30–15-day, and 15–7.5-day bandpass-filtered deep-ocean η_{5300}. (left) Spatial amplitude normalized by the maximum value, with contour interval 0.1. (right) Phase, with contour interval 30°. (bottom) Amplitude time series corresponding to the first mode spatial amplitude.

indicates that propagation characteristics are the same during stable and unstable periods.

Phase speeds determined by other investigators for meanders in the Kuroshio Extension are also shown in Fig. 11 for comparison. Both Mizuno (1985) and Kouketsu et al. (2007) reported slower phase speeds than ours for the shorter-wavelength meanders. However, their estimates have limitations: Both studies examined only a few meanders and Kouketsu et al. (2007) had the additional complication that phase speed was indirectly estimated by relocating hydrographic station data. Propagation speeds were also determined by Hirai (1985) for frontal eddies. His estimates of 35–45 cm s^{-1} are not plotted because neither wavelengths nor periods were provided.

Insight as to why the meander phase speeds differ between the previous studies and ours comes from the KESS dataset itself. The slowly propagating, fast-growing meander crests with wavelengths of roughly 200 km tracked by Mizuno (1985) in the SST images are composites of shorter-wavelength meanders propagating rapidly along a slowly propagating, fast-growing meander with a wavelength greater than 400 km. Figure 12 illustrates an example from KESS that is similar to the three cases presented in Mizuno (1985). The η_{upper} fields for four dates during November–December 2004 at 10-day intervals are superimposed on SST images, illustrating that the satellite and KESS measurements provide consistent positions for the Kuroshio Extension path. The $\eta_{\text{upper}} = 3.9$ m contour from these panels are redisplayed in Fig. 12e by the black lines together with the paths on the intervening dates. Dotted lines track two crests as they propagate downstream. The distance between these crests provides an estimate of 270 km for wavelength. A mean phase speed of 7.3 km day^{-1} was estimated for the western crest. These λ and c estimates are comparable to those in Mizuno (1985). His figures also show nonuniform phase speeds for the crests like those in Fig. 12e. The subsequent panels (Figs. 12f–i) show these path displacements after they were low-pass filtered with a cutoff period of 60 days (Fig. 12f) and bandpass-filtered η_{upper} anomalies tracked along a mean path determined for this time period (Figs. 12g–i). The 60-day low-pass-filtered paths reveal a fast-growing meander propagating slowly at roughly 3 km day^{-1}, but with a much longer wavelength ($\lambda \sim 380$–580 km). Furthermore, the along-path anomalies reveal several shorter-wavelength meanders propagating along the path at higher speeds consistent with our previous analyses. (For clarity, only the first 500 km of the along-path distance is plotted.) The phase speeds inferred in Fig. 12e are therefore shown to have contributions from both the long-period and short-period meanders. With his dataset, Mizuno (1985) was unable to distinguish the contributions of the various frequencies.

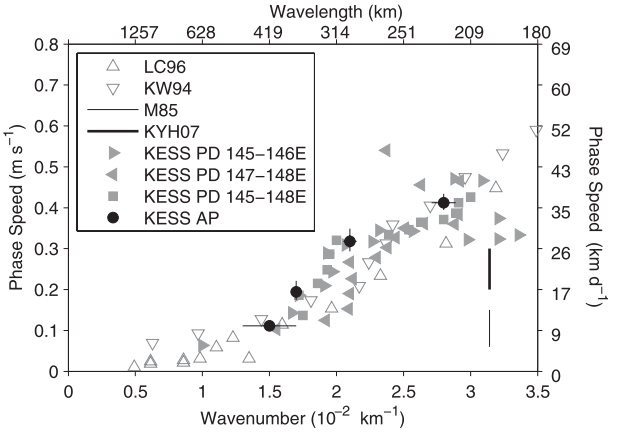

FIG. 11. Comparison of several dispersion relationships derived for the Kuroshio Extension and the Gulf Stream. Solid symbols are phase speeds derived from KESS using the path-displacement (gray) and along-path (black) η_{upper} methods. Gulf Stream values (open symbols) were determined by Kontoyiannis and Watts (1994) and Lee and Cornillon (1996). Additional values for the Kuroshio Extension (solid lines) were reported by Mizuno (1985) and Kouketsu et al. (2007).

The empirical relation for Kuroshio Extension meanders shown in Fig. 11 exhibits a parabolic shape of the form $c(k) = Ak^2 - B$, which is consistent with the thin jet theory of Cushman-Roisin et al. (1993). Coefficients A and B were related by Cushman-Roisin et al. (1993) and Lee and Cornillon (1996) to the vertical and lateral structure of the current. Empirical dispersion relationships determined for Gulf Stream meanders using inverted echo sounder data by Kontoyiannis and Watts (1994) and satellite infrared imagery by Lee and Cornillon (1996) exhibit this same parabolic shape (Fig. 11). Phase speeds predicted by Kouketsu and Yasuda (2008) for the most unstable waves in the Kuroshio Extension using a linear stability analysis are consistently ~60% smaller than the values observed during KESS.

The KESS estimates for high-wavenumber/short-period meanders from the path-displacement method are more scattered than those estimated for the Gulf Stream. The increased scatter is likely due to two sources. First, as noted above and illustrated in the appendix, the amplitudes of meanders with $\lambda \leq 220$ km are not well resolved by the KESS array. Second, the slowest of these phase-speed estimates were calculated using the 145°–146°E longitude pair. An instrument located in that region failed during the first year, creating a larger gap between measurement sites, which produces an area within the η_{upper} fields with higher mapping error (Fig. 3). The along-path estimate for the short-period meanders is

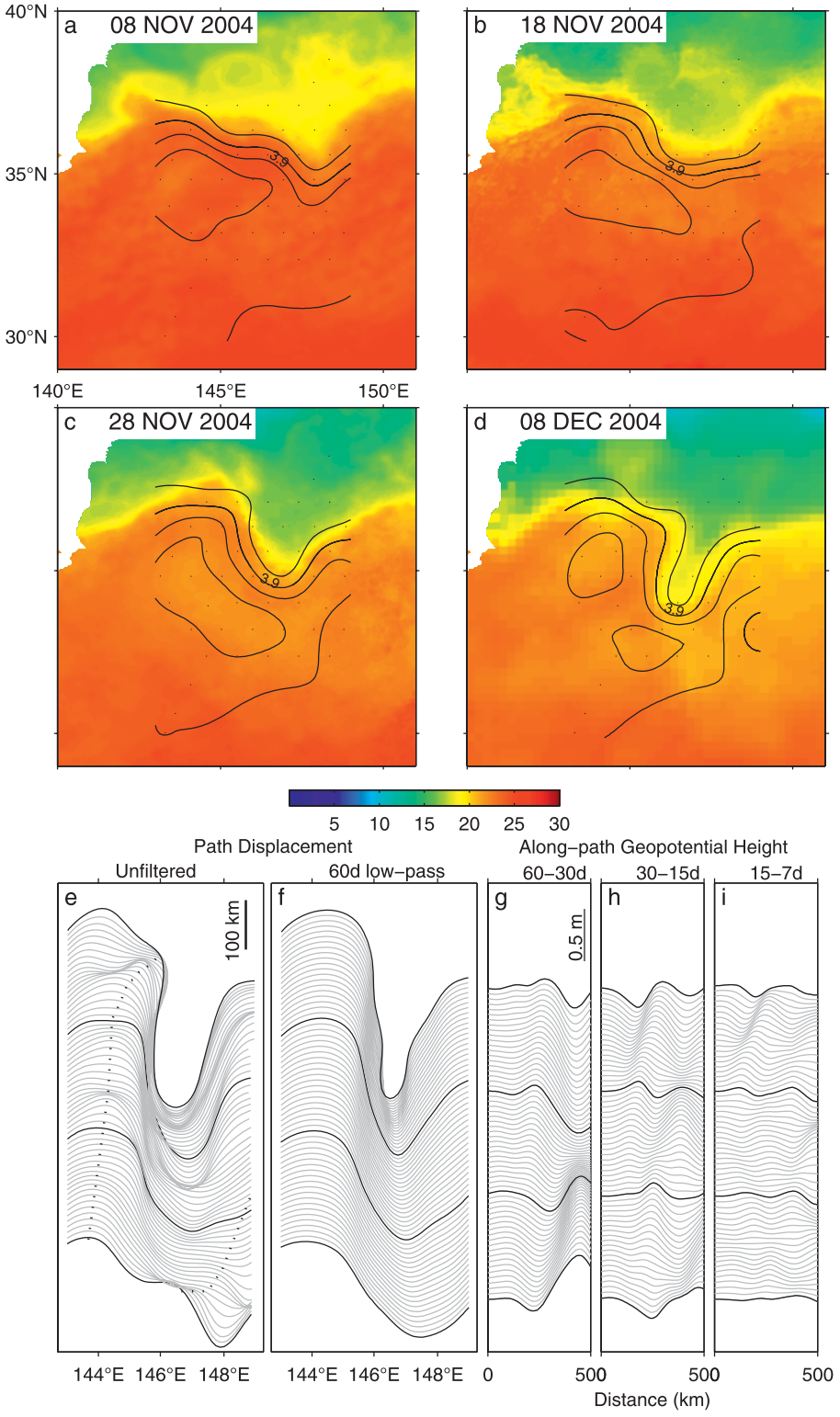

FIG. 12. A rapidly growing meander. (a)–(d) η_{upper} (contour interval 0.4 m) superimposed on NGSST-O SST maps (°C) are shown for four dates. (e) Unfiltered displacements of the 3.9-m contour relative to 35°N at 0.5-day intervals. The paths corresponding to the dates in (a)–(d) are plotted in black. Dotted lines indicate phase propagation of two crests. (f) 60-day low-pass-filtered path displacements. Along-path η_{upper} bandpass filtered in three period bands, (g) 60–30 days, (h) 30–15 days, and (i) 15–7.5 days. Line origins are shifted such that time increases upward in each panel. The distance scale in (e) applies to (f), and the amplitude scale in (g) applies to (h) and (i).

insensitive to this problem because the wavenumber was calculated over a longer distance.

e. Meander growth

Although Kuroshio Extension and Gulf Stream meanders have similar propagation speeds, they differ in how they amplify. Watts and Johns (1982) and Tracey and Watts (1986) found Gulf Stream meanders just downstream of Cape Hatteras grew continuously out to 72°W, with spatial and temporal *e*-folding scales comparable to the meander wavelengths and periods. In contrast, in the KESS region, although continuous growth was observed for a few individual propagating meanders (Fig. 7), it was more common for growth to occur for brief intervals over short distances because of the presence of eddies in the deep ocean. Meanders intensified when they encountered deep, nearly depth-independent eddies crossing the upper jet only if a vertical phase offset existed that favored baroclinic instability. As the upper meanders and deep eddies moved past each other, their orientation changed such that it no longer favored instability, and growth ceased (Fig. 8). Because of these interactions with the deep eddies, estimating spatial and temporal meander growth rates as was done for the Gulf Stream by Watts and Johns (1982) and Tracey and Watts (1986) or for the Kuroshio Extension by Kouketsu and Yasuda (2008) is not applicable for most of the meanders observed during KESS.

Greene (2010) evokes the self-development model of Sutcliffe (1947) to provide the dynamical interpretation for the intensification observed in the 60–30-day band during KESS. The basic argument requires that the centers of the upper and deep anomalies of finite amplitude be spatially offset, which causes water parcels to be advected across the front. In the case of a deep anticyclone offset downstream of a meander crest, water parcels entering the crest in the upper layer are squashed as they are advected northward where they gain negative relative vorticity, and the crest intensifies. This, in turn, deepens the pycnocline and squashes the lower layer where the water parcels gain negative relative vorticity, causing the deep anticyclone to intensify as well. The same scenario, but of opposite sign, can be invoked to explain the joint spinup of meander troughs and deep cyclones. A similar argument can be applied to the intensification observed herein for meanders in other period bands. Greene (2010) points out that in some respects this mechanism is similar to the joint spinup events observed in the Gulf Stream (Shay et al. 1995; Savidge and Bane 1999). He notes, however, that in those cases pressure anomalies under the Gulf Stream grew locally to large amplitude from small-amplitude perturbations, whereas, under the Kuroshio Extension, deep pressure anomalies of appreciable amplitude propagated into the KESS array from an external source region. Figures 6–8 illustrate that these same processes of vertical coupling and self-development are active in shorter-period bands.

7. Summary

Meanders with periods shorter than 60 days were observed propagating downstream along the Kuroshio Extension between 143° and 149°E from June 2004 through September 2005. The KESS moored array provided synoptic measurements of the upper and deep fluctuations with mesoscale resolution. Meanders, also called frontal waves, were observed transiting the array continually during the 16-month program. Propagation speeds were estimated by two methods, spectral analysis of path displacements and CEOF analysis of along-path anomalies, producing consistent results. Phase speeds increased with frequency and wavenumber from 10 to 35 km day^{-1} for meanders with wavelengths and periods from [420 km, 40 days] to [220 km, 6 days], respectively. The empirical relationship between phase speed and wavenumber is remarkably indistinguishable from that obtained for Gulf Stream meanders despite the subtle differences between the two current systems. This result differs from previous studies, which reported smaller phase speeds for meanders with wavelength ~200 km in the Kuroshio Extension than in the Gulf Stream. The KESS dispersion relation is an improvement over those earlier studies because it is based on considerably more data with well-suited spatiotemporal resolution.

Steady downstream growth was uncommon for meanders in the KESS region. More often than not, growth was intermittent because preexisting eddies in the deep ocean have a significant influence upon meander intensification. Growth occurred locally when upper meanders encountered deep, nearly depth-independent eddies of external origin with the right phase offset; the deep eddy center shifted about 1/8–1/4 wavelength downstream of the upper. Growth ceased when this phase offset changed as they moved past each other.

Future theoretical or modeling studies of meander growth and propagation should account for more than the velocity, density, and potential vorticity structure in the Kuroshio Extension. Instead, they must include frequent encounters with the nearly depth-independent eddies that populate this region.

Acknowledgments. The CPIES were developed and prepared by G. Chaplin and E. Sousa with assistance from C. Cipolla and G. Savoy at the URI Equipment

Development Laboratory. M. Kennelly assisted with the initial processing of the CPIES records. We are grateful to A. Greene for processing the travel-time records from calibration through mapping and for generating the hydrographic lookup tables. We appreciate the additional KESS current meter data supplied by our colleagues N. Hogg, S. Jayne, and L. Rainville. The ASUKA PIES data were obtained online from the Ocean-Atmosphere Interaction Research Team of the Japan Agency for Marine-Earth Science and Technology. This work was supported by the National Science foundation as part of the Kuroshio Extension System Study (OCE-0221008 and 0851246).

APPENDIX

Propagating-Meander Detection by KESS

Simulations were conducted to determine how well the KESS array resolves propagating meanders given the instrument spacing of 88 km and the Gaussian correlation-length scale of 75 km that had been determined from the observations and used for the objective mapping of η_{upper}. Meanders were simulated as symmetric, eastward-propagating, geopotential-height anomalies η with time-variable amplitudes A on a high-resolution grid. Multiple simulations were run using a suite of wavelengths λ, periods T, and phase speeds c based on the KESS estimates listed in Tables 1 and 2.

The anomalies were prescribed as

$$\eta(x, y, t) = A \cos\left[\frac{2\pi(y - y_o)}{\lambda}\right] \cos\left[\frac{2\pi(x - ct)}{\lambda}\right],$$

where y_o is the meridional location of the anomaly centers and t is elapsed time. Simulations were run with $y_o = y_{\text{cpies}} + \Delta y$, where y_{cpies} is the mean meridional position of a line of instruments and Δy allows the anomalies to be offset from the sites. Amplitude was specified as either a constant $A = A_o$ or time varying,

$$A(t) = A_o[(1 - \alpha) + \alpha \sin(2\pi t/T_o)],$$

where $A_o = 0.3$ m is a typical amplitude for the observed anomalies and $\alpha = 0.4$ and T_o set the magnitude and period of modulation. Daily analytic fields were generated on an x, y grid with 4-km spacing and spanning the length and width of the main KESS array. Each simulation ran for 100 days. Snapshots of the analytic η fields at the initialization of each run are shown in the left-hand column of Fig. A1 for four [λ, T, c] cases. For the simulations shown in these examples, $\Delta y = 44$ so that the anomalies were centered midway between the instrumented lines and their amplitudes modulated with $T_o = 50$ days. Subsequently, each analytic field was subsampled at the CPIES locations (shown by the diamonds) and remapped on to the x, y grid with the same procedures used for the KESS data (Donohue et al. 2010).

Meander periods, wavelengths, and phase speeds were determined from both the analytic and mapped fields using the along-path method described in section 4. For each simulation, geopotential-height anomalies η were extracted from both the analytic and mapped fields along a chosen mean path y_{mp} for each time step and Hovmöller diagrams were generated. Various combinations of y_o and y_{mp} were tested, and Fig. A1 illustrates a worst case scenario, meanders of variable amplitude located halfway between the instrumented lines. In these plots, η contours sloping from the lower left to the upper right indicate downstream propagation. Here, T and λ were calculated from the computed CEOF mode spatial and temporal phases, respectively. Accurate slopes were obtained from the unwrapped spatial phases by averaging over distances of 300–400 km. Propagation speeds were calculated from T and λ.

The results for the simulations shown in Fig. A1 are tabulated in Table A1. There is near perfect agreement between the analytic and mapped periods, and the wavelengths differ by less the 1.5%. In most of the simulations, the mapped wavelengths were slightly underestimated for $\lambda > 250$ km and slightly overestimated for $\lambda < 250$ km. The corresponding phase speeds are as accurate as the estimated T and λ.

Variations in the amplitudes of the anomalies were examined at several fixed locations along the mean paths. In the right-hand column of Fig. A1, the analytic and mapped η at $x = 0$ are plotted as a function of time. Amplitudes are well resolved for the longer-wavelength meanders. For $\lambda = 250$ km, the amplitudes are adequately resolved, with mapped $\eta \approx 70\%$ of analytic η. Amplitudes of short-wavelength meanders (180 km $\leq \lambda \leq 220$ km) are poorly resolved in the simulation shown in Fig. A1; mapped η are only 1/3 of analytic η. In other simulations where the anomalies were centered over the instrumented lines ($y_o = y_{\text{cpies}}$) and the mean path was off center ($y_{\text{mp}} \neq y_o$), the mapped η values could be as much as 3 times bigger than the analytic values; mapping stretched the meridional extent of such small-scale anomalies if they happened to pass exactly over a measurement site. Amplitudes of the short-wavelength anomalies were well resolved when both their centers and the mean path coincided with the instrumented lines ($y_o = y_{\text{mp}} = y_{\text{cpies}}$). Regardless of these uncertainties, the analysis of meander growth presented in section 5 is

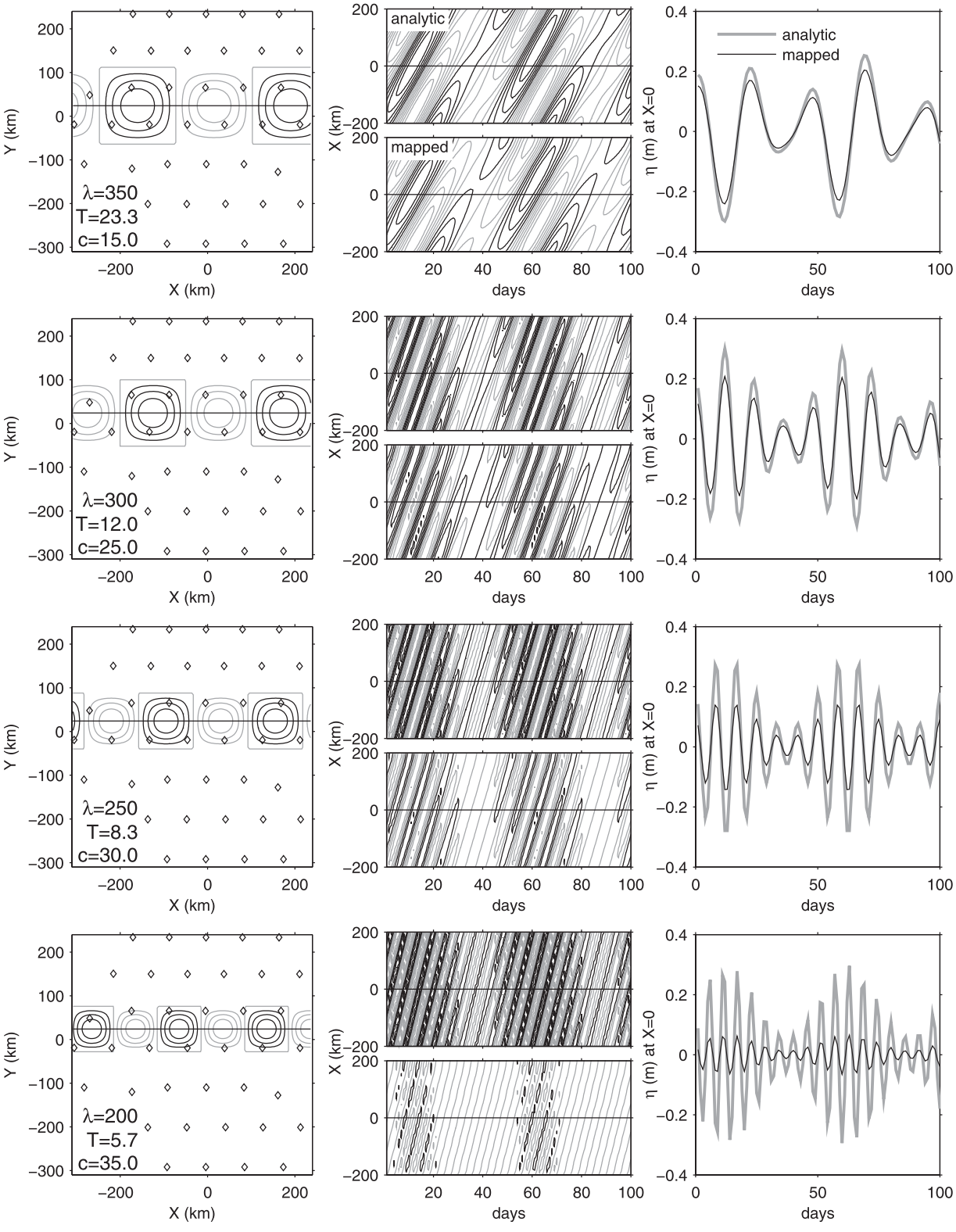

FIG. A1. Simulations of propagating anomalies in which their centers are located midway between the instrumented lines. Each row corresponds to a different [λ, T, c] simulation. (left) Analytic η field at initialization. Positive anomalies are gray, and negative anomalies are black. Contour interval is 0.05 m. The horizontal line shows the mean path y_{mp} chosen for these simulations. (middle) Hovmöller diagrams of analytic (upper) and mapped (lower) η as functions of along-path distance and time. (right) Time series of analytic (gray) and mapped (black) η at $x = 0$.

TABLE A1. Comparison of the periods T, wavelengths λ, and phase speeds c calculated for the analytic and mapped fields for the simulations shown in Fig. A1 in which both the anomalies and mean path were located midway between the instrumented lines.

Analytic			Mapped		
T (days)	λ (km)	c (km day^{-1})	T (days)	λ (km)	c (km day^{-1})
23.4	350	15.0	23.4	353	15.1
12.0	300	25.0	12.0	304	25.3
8.3	250	30.0	8.3	254	30.4
5.7	200	35.0	5.7	203	35.6

not affected, because it examined meanders with wavelengths greater than 250 km.

Finally, propagating features in the deep-ocean η_{5300} fields will be even better resolved, because pressure and its gradients were used as inputs for mapping. Additionally, the deep correlation-length scale of 100 km was larger than that for η_{upper}. These findings scale with the ratio of correlation length to simulated-eddy scale. The combined effect of these indicates that deep eddies with $\lambda = 220$ km would be mapped as well as the upper-ocean anomalies with $\lambda = 350$ km shown in Fig. A1 (top).

REFERENCES

Ambe, D., S. Imawaki, H. Uchida, and K. Ichikawa, 2004: Estimating the Kuroshio axis south of Japan using combination of satellite altimetry and drifting buoys. *J. Oceanogr.,* **60,** 375–382.

Bane, J. M., D. A. Brooks, and K. R. Lorenson, 1981: Synoptic observations of the three-dimensional structure and propagation of Gulf Stream meanders along the Carolina continental margin. *J. Geophys. Res.,* **86,** 6411–6425.

Book, J. W., M. Wimbush, S. Imawaki, H. Ichikawa, H. Uchida, and H. Kinoshita, 2002: Kuroshio temporal and spatial variations south of Japan determined from inverted echo sounder measurements. *J. Geophys. Res.,* **107,** 3121, doi:10.1029/2001JC000795.

Chen, S., B. Qiu, and P. Hacker, 2007: Profiling float measurements of the recirculation gyre south of the Kuroshio Extension in May to November 2004. *J. Geophys. Res.,* **112,** C05023, doi:10.1029/2006JC004005.

Cushman-Roisin, B., L. Pratt, and E. Ralph, 1993: A general theory for eqivalent barotropic thin jets. *J. Phys. Oceanogr.,* **23,** 91–103.

Donohue, K. A., and Coauthors, 2008: Program studies the Kuroshio Extension. *Eos, Trans. Amer. Geophys. Union,* **89,** 161–162.

——, D. R. Watts, K. L. Tracey, A. D. Greene, and M. Kennelly, 2010: Mapping circulation in the Kuroshio Extenstion with an array of current and pressure recording inverted echo sounders. *J. Atmos. Oceanic Technol.,* **27,** 507–527.

Greene, A. D., 2010: Deep variability in the Kuroshio Extension. Ph.D. thesis, University of Rhode Island, 150 pp.

Halliwell, G. R., and C. N. K. Mooers, 1983: Meanders of the Gulf Stream downstream from Cape Hatteras 1975–1978. *J. Phys. Oceanogr.,* **13,** 1275–1292.

Hannachi, A., I. T. Jolliffe, and D. B. Stephenson, 2007: Empirical orthogonal functions and related techniques in atmospheric science: A review. *Int. J. Climatol.,* **27,** 1119–1152.

Hirai, M., 1985: Satellite observation of characteristic features of frontal eddies in the vicinity of the Kuroshio front. *Bull. Tohoku Reg. Fish. Res. Lab.,* **47,** 69–78.

Hogg, N. G., R. S. Pickart, R. M. Hendry, and W. J. S. Jr., 1986: The northern recirculation gyre of the Gulf Stream. *Deep-Sea Res.,* **33,** 1139–1165.

Howe, P. J., K. A. Donohue, and D. R. Watts, 2009: Stream-coordinate structure and variability of the Kuroshio Extension. *Deep-Sea Res. I,* **56,** 1093–1116, doi:10.1016/j.dsr.2009.03.007.

Jayne, S. R., and Coauthors, 2009: The Kuroshio Extension and its recirculation gyres. *Deep-Sea Res. I,* **56,** 2088–2099.

Johns, W. E., T. J. Shay, J. M. Bane, and D. R. Watts, 1995: Gulf Stream structure, transport, and recirculation near 68°W. *J. Geophys. Res.,* **100,** 817–838.

Kakinoki, K., and Coauthors, 2008: Variations of Kuroshio geostrophic transport south of Japan estimated from long-term IES observations. *J. Oceanogr.,* **64,** 373–384.

Kennelly, M., K. Tracey, and D. R. Watts, 2007: Inverted echo sounder data processing manual. University of Rhode Island Graduate School of Oceanography Tech. Rep. 2007-02, 87 pp. [Available online at http://digitalcommons.uri.edu/physical_oceanography_techrpts/2/.]

——, K. Donohue, A. Greene, K. L. Tracey, and D. R. Watts, 2008: Inverted echo sounder data report: Kuroshio Extension System Study (KESS), April 2004 to July 2006. University of Rhode Island Graduate School of Oceanography Tech. Rep. 2008-2, 69 pp. [Available online at http://digitalcommons.uri.edu/physical_oceanography_techrpts/1/.]

Kontoyiannis, H., and D. R. Watts, 1994: Observations on the variability of the Gulf Stream path between 74°W and 70°W. *J. Phys. Oceanogr.,* **24,** 1999–2013.

Kouketsu, S., and I. Yasuda, 2008: Unstable frontal waves along the Kuroshio Extension with low-potential vorticity intermediate Oyashio water. *J. Phys. Oceanogr.,* **38,** 2308–2321.

——, ——, and Y. Hiroe, 2005: Observations of frontal waves and associated salinity minimum formation along the Kuroshio Extension. *J. Geophys. Res.,* **110,** C08011, doi:10.1029/2004JC002862.

——, ——, and ——, 2007: Three-dimensional struture of frontal waves and associated salinity minimum formation along the Kuroshio Extension. *J. Phys. Oceanogr.,* **37,** 644–656.

Lee, T., and P. Cornillon, 1996: Propagation of Gulf Stream meanders between 74° and 70°W. *J. Phys. Oceanogr.,* **26,** 205–224.

Lee, T. N., L. P. Atkinson, and R. Legeckis, 1981: Observations of a Gulf Stream frontal eddy on the Georgia continental shelf, April 1977. *Deep-Sea Res.,* **28,** 347–378.

Meinen, C. S., D. S. Luther, and M. O. Baringer, 2009: Structure, transport and potential vorticity of the Gulf Stream at 68°W: Revisiting older data sets with new techniques. *Deep-Sea Res. I,* **56,** 41–60, doi:10.1016/j.dsr.2008.07.010.

Mizuno, K., 1985: Some examples of short term fluctuations in the Kuroshio Extension detected by IR imagery. *Bull. Tohoku Reg. Fish. Res. Lab.,* **47,** 59–68.

——, and W. White, 1983: Annual and interannual variability in the Kuroshio current system. *J. Phys. Oceanogr.,* **13,** 1847–1867.

Qiu, B., and S. Chen, 2005: Variability of the Kuroshio Extension jet, recirculation gyre, and mesoscale eddies on decadal time scales. *J. Phys. Oceanogr.,* **35,** 2090–2103.

——, ——, P. Hacker, N. G. Hogg, S. R. Jayne, and H. Sasaki, 2008: The Kuroshio Extension northern recirculation gyre: Profiling float measurements and forcing mechanism. *J. Phys. Oceanogr.,* **38,** 1764–1779.

Sakaida, F., H. Kawamura, S. Takahashi, T. Shimada, Y. Kawai, K. Hosoda, and L. Guan, 2009: Research and development of the New Generation Sea Surface Temperature for Open Ocean (NGSST-O) product and its demonstration operation. *J. Oceanogr.,* **65,** 859–870.

Savidge, D. K., and J. M. Bane, 1999: Cyclogenesis in the deep ocean beneath the Gulf Stream 2. Dynamics. *J. Geophys. Res.,* **104,** 18 127–18 140.

Shay, T. J., J. M. Bane, D. R. Watts, and K. L. Tracey, 1995: Gulf Stream flow field and events near 68°W. *J. Geophys. Res.,* **100,** 22 565–22 589.

Sutcliffe, R. C., 1947: A contribution to the problem of development. *Quart. J. Roy. Meteor. Soc.,* **73,** 370–383.

Tatebe, H., and I. Yasuda, 2001: Seasonal axis migration of the upstream Kuroshio Extension associated with standing oscillations. *J. Geophys. Res.,* **106,** 16 685–16 692.

Tracey, K. L., and D. R. Watts, 1986: On Gulf Stream meander characteristics. *J. Geophys. Res.,* **91,** 7587–7602.

Watts, D. R., and W. E. Johns, 1982: Gulf Stream meanders: Observations on propagation and growth. *J. Geophys. Res.,* **87,** 9467–9476.